

## A FOURTH ORDER DIFFERENCE SCHEME FOR THE MAXWELL EQUATIONS ON YEE GRID

ALY FATHY

*Department of Electrical and Computer Engineering  
University of Tennessee, Knoxville, TN 37996-2100, USA  
fathy@ece.utk.edu*

CHENG WANG

*Department of Mathematics, University of Massachusetts Dartmouth  
North Dartmouth, MA 02747-2300, USA  
wang@math.utk.edu*

JOSHUA WILSON

*Spallation Neutron Source/Research Accelerator Division  
Oak Ridge National Laboratory, Oak Ridge, TN 37831, USA  
wilsonjl@ornl.gov*

SONGNAN YANG

*Department of Electrical and Computer Engineering  
University of Tennessee, Knoxville, TN 37996-2100, USA  
syang4@utk.edu*

Received 7 Sep. 2007  
Accepted 17 Oct. 2007

Communicated by Jian-Guo Liu

**Abstract.** The Maxwell equations are solved by a long-stencil fourth order finite difference method over a Yee grid, in which different physical variables are located at staggered mesh points. A careful treatment of the numerical values near the boundary is introduced, which in turn leads to a “symmetric image” formula at the “ghost” grid points. Such a symmetric formula assures the stability of the boundary extrapolation. In turn, the fourth order discrete curl operator for the electric and magnetic vectors gives a complete set of eigenvalues in the purely imaginary axis. To advance the dynamic equations, the four-stage Runge–Kutta method is utilized, which results in a full fourth order accuracy in both time and space. A stability constraint for the time step is formulated at both the theoretical and numerical levels, using an argument of stability domain. An accuracy check is presented to verify the fourth order precision, using a comparison between exact solution and numerical solutions at a fixed final time. In addition, some numerical simulations of a loss-less rectangular cavity are also carried out and the frequency is measured precisely.

*Keywords:* Maxwell equations; Yee grid; long stencil fourth order approximation; “symmetric image” formula; Jameson method; stability domain.

Mathematics Subject Classification 2000: 35F10, 35L45, 35P05, 65M06, 65M12

## 1. Introduction

Time domain simulation of electromagnetic fields is of great practical significance in engineering and physics, since it allows a broad spectrum of frequencies to be analyzed in a single simulation. The classical central difference scheme introduced by Yee [22] proved to be second order accurate in space and time. As always in the case of a second order method, the Yee scheme begins to accumulate phase errors as time grows large, especially for electrically large domains or for late-time analysis. Because of this, a number of attempts have been made to extend this scheme to fourth order accuracy since Fang’s pioneering work [2]. Fourth order methods allow a coarser time step and spatial mesh to be used while maintaining the same accuracy (effectively increasing simulation speed), or can increase the accuracy for a given mesh spacing and time step.

A direct application of a fourth order long-stencil difference results in a one-sided approximation formula around the boundary, such as a fourth order closure proposed in Petropoulos and Yefet [12] and relevant works [3, 4, 11, 13, 16], etc. An alternate approach to overcome the boundary difficulties is to introduce a compact difference operator for the spatial derivatives over the Yee stencil, as discussed in detail in Young [26]. Unfortunately, these conventional approaches of fourth order methods tend to suffer from instability near the boundary or require an implicit updating scheme. Additionally, the fourth order leap-frog or the classic fourth order Runge–Kutta method (RK4) is typically used for the fourth order time integration. The fourth order leap frog scheme leads to a corrective derivative that is very complicated to implement. The RK4 integrator requires the storage of many temporary, intermediate field values, which increases the memory storage requirements drastically over the second order method. Discussions of other fourth order *FDTD* schemes and related issues can also be found in [1, 20, 21, 23, 24, 27], etc.

In this paper, a fully explicit fourth order scheme over the Yee mesh grid is proposed, which does not suffer from instability near the boundary. Different physical variables representing electric and magnetic vectors are located at different mesh points. Such a staggered grid makes the computed vectors divergence-free at a discrete level. The extrapolation formulas near the boundary are very simple to implement. (Here, the treatment of boundary conditions is demonstrated for a perfectly conducting rectangular domain, but the principles can be extended to accommodate other types of boundary conditions.) This article is the first to demonstrate a fourth order accuracy using a “symmetric image” formula. In addition, the time integration is done using Jameson method, a four-stage integrator that is improved from the commonly used RK4 integrator in that fewer temporary storage variables are required, saving memory. Such a time integration, proposed

by Jameson in [7, 8] in the numerical simulations of gas dynamics, is only second order accurate for nonlinear equations. It is the first time the Jameson method has been applied to the computation of electromagnetic fields. The resulting scheme is shown to preserve fourth order accuracy in space and time for the linear Maxwell equations. At the same time, it offers a larger stability domain than the second order scheme. It is shown that the corresponding *CFL* number can be improved over that of the second order leap-frog scheme by a factor of  $2\sqrt{2}$ . Meanwhile, the long stencil difference operator leads to an eigenvalue with a maximum magnitude of  $\frac{7}{6}$  times that of the classical (second order) central difference. As a result, the overall fourth order scheme has a maximum *CFL* number of  $\frac{12\sqrt{2}}{7}$ , which is a drastic improvement.

The article is organized as follows. In Sec. 2, we review the formulation of the Maxwell equations and formulate the eigenvalues and eigenfunctions of the curl operator at the continuous level. In Sec. 3, we describe the fourth order scheme in detail, including both the spatial and temporal discretizations. In Sec. 4, an exact solution with a single mode is studied and computed by the proposed scheme. An accuracy check is performed by a comparison between the exact and numerical solutions at a given time instant, which in turn shows a full fourth order accuracy. In Sec. 5, we compute a physical example of a loss-less rectangular cavity. Different modes are included in the initial data with a decaying magnitude. An *FFT* tool is utilized to analyze the frequency of the wave over time. This shows that the proposed  $4 \times 4$  scheme performs much better than the classical  $2 \times 2$  and  $2 \times 4$  methods in the accuracy of resonant frequency computations.

## 2. The Formulation

We denote  $\mathbf{E} = (E_x, E_y, E_z)^T$ ,  $\mathbf{H} = (H_x, H_y, H_z)^T$  as the electric field and the magnetic field, respectively. Over a 3-D domain  $\Omega \subset R^3$ , the Maxwell equations take the form of

$$\left\{ \begin{array}{l} \partial_t \mathbf{E} = \frac{1}{\epsilon} \nabla \times \mathbf{H} = \frac{1}{\epsilon} \begin{pmatrix} \partial_y H_z - \partial_z H_y \\ \partial_z H_x - \partial_x H_z \\ \partial_x H_y - \partial_y H_x \end{pmatrix}, \\ \partial_t \mathbf{H} = -\frac{1}{\mu} \nabla \times \mathbf{E} = -\frac{1}{\mu} \begin{pmatrix} \partial_y E_z - \partial_z E_y \\ \partial_z E_x - \partial_x E_z \\ \partial_x E_y - \partial_y E_x \end{pmatrix}, \\ \nabla \cdot \mathbf{E} = 0, \\ \nabla \cdot \mathbf{H} = 0, \end{array} \right. \quad (2.1)$$

in which  $\mu, \epsilon > 0$  represent magnetic permeability and electric permittivity, respectively. As a result, the speed of light is given by  $c = \sqrt{\frac{1}{\mu\epsilon}}$ . The perfectly conducting

boundary conditions are imposed as

$$\begin{aligned} \mathbf{E} \cdot \boldsymbol{\tau} &= 0, & \frac{\partial(\mathbf{E} \cdot \mathbf{n})}{\partial \mathbf{n}} &= 0, & \text{on } \partial\Omega, \\ \mathbf{H} \cdot \mathbf{n} &= 0, & \frac{\partial(\mathbf{H} \cdot \boldsymbol{\tau})}{\partial \mathbf{n}} &= 0, & \text{on } \partial\Omega, \end{aligned} \tag{2.2}$$

in which  $\mathbf{n}$  and  $\boldsymbol{\tau}$  represent the unit normal and tangential vectors on the boundary, respectively. Note that the second part of (2.2) comes from an application of the divergence-free constraint for both  $\mathbf{E}$  and  $\mathbf{H}$  on the boundary.

We note that each component of  $\mathbf{E}$  and  $\mathbf{H}$  satisfies the wave equation:

$$\partial_t^2 E_i = \frac{1}{\mu\epsilon} (\partial_x^2 + \partial_y^2 + \partial_z^2) E_i, \quad \partial_t^2 H_i = \frac{1}{\mu\epsilon} (\partial_x^2 + \partial_y^2 + \partial_z^2) H_i, \quad \text{for } i = 1, 2, 3. \tag{2.3}$$

The above wave equations come from the following identity

$$\nabla \times (\nabla \times \mathbf{u}) = -\Delta \mathbf{u} + \nabla(\nabla \cdot \mathbf{u}), \tag{2.4}$$

for any  $\mathbf{u} \in R^3$ .

In a cubic rectangular domain  $\Omega = (0, a_1) \times (0, a_2) \times (0, a_3)$ , we observe the following profile

$$\begin{aligned} E_x &= A_1 \cos\left(\frac{l\pi x}{a_1}\right) \sin\left(\frac{m\pi y}{a_2}\right) \sin\left(\frac{n\pi z}{a_3}\right), \\ E_y &= A_2 \sin\left(\frac{l\pi x}{a_1}\right) \cos\left(\frac{m\pi y}{a_2}\right) \sin\left(\frac{n\pi z}{a_3}\right), \\ E_z &= A_3 \sin\left(\frac{l\pi x}{a_1}\right) \sin\left(\frac{m\pi y}{a_2}\right) \cos\left(\frac{n\pi z}{a_3}\right), \\ H_x &= B_1 \sin\left(\frac{l\pi x}{a_1}\right) \cos\left(\frac{m\pi y}{a_2}\right) \cos\left(\frac{n\pi z}{a_3}\right), \\ H_y &= B_2 \cos\left(\frac{l\pi x}{a_1}\right) \sin\left(\frac{m\pi y}{a_2}\right) \cos\left(\frac{n\pi z}{a_3}\right), \\ H_z &= B_3 \cos\left(\frac{l\pi x}{a_1}\right) \cos\left(\frac{m\pi y}{a_2}\right) \sin\left(\frac{n\pi z}{a_3}\right), \end{aligned} \tag{2.5}$$

is divergence-free and satisfies the boundary condition (2.2) for any  $l, m, n \in Z$ , if the following constraints for the coefficients are imposed

$$\bar{l}A_1 + \bar{m}A_2 + \bar{n}A_3 = 0, \quad \bar{l}B_1 + \bar{m}B_2 + \bar{n}B_3 = 0, \quad \text{with} \tag{2.6a}$$

$$\bar{l} = \frac{l\pi}{a_1}, \quad \bar{m} = \frac{m\pi}{a_2}, \quad \bar{n} = \frac{n\pi}{a_3}. \tag{2.6b}$$

Moreover, they form a complete set of eigenfunctions of the operator in (2.1) provided that

$$\begin{aligned}
 -\frac{1}{\epsilon}(\bar{m}B_3 - \bar{n}B_2) &= \lambda A_1, & -\frac{1}{\epsilon}(\bar{n}B_1 - \bar{l}B_3) &= \lambda A_2, \\
 -\frac{1}{\epsilon}(\bar{l}B_2 - \bar{m}B_1) &= \lambda A_3, & -\frac{1}{\mu}(\bar{m}A_3 - \bar{n}A_2) &= \lambda B_1, \\
 -\frac{1}{\mu}(\bar{n}A_1 - \bar{l}A_3) &= \lambda B_2, & -\frac{1}{\mu}(\bar{l}A_2 - \bar{m}A_1) &= \lambda B_3.
 \end{aligned} \tag{2.7}$$

Additionally, by setting  $\bar{\lambda}_{l,m,n} = \sqrt{(\bar{l})^2 + (\bar{m})^2 + (\bar{n})^2}$ , we have the following eigenvalues (with  $\mathbf{i} = \sqrt{-1}$ )

$$\begin{aligned}
 A_1 &= \sqrt{\frac{1}{\epsilon}}, & A_2 &= \sqrt{\frac{1}{\epsilon}} \cdot \frac{-\bar{l}\bar{m} + \bar{n}\bar{\lambda}_{l,m,n}\mathbf{i}}{(\bar{m})^2 + (\bar{n})^2}, & A_3 &= \sqrt{\frac{1}{\epsilon}} \cdot \frac{-\bar{l}\bar{n} - \bar{m}\bar{\lambda}_{l,m,n}\mathbf{i}}{(\bar{m})^2 + (\bar{n})^2}, \\
 B_1 &= \sqrt{\frac{1}{\mu}}, & B_2 &= \sqrt{\frac{1}{\mu}} \cdot \frac{-\bar{l}\bar{m} + \bar{n}\bar{\lambda}_{l,m,n}\mathbf{i}}{(\bar{m})^2 + (\bar{n})^2}, & B_3 &= \sqrt{\frac{1}{\mu}} \cdot \frac{-\bar{l}\bar{n} - \bar{m}\bar{\lambda}_{l,m,n}\mathbf{i}}{(\bar{m})^2 + (\bar{n})^2} \\
 \lambda &= \sqrt{\frac{1}{\mu\epsilon} ((\bar{l})^2 + (\bar{m})^2 + (\bar{n})^2)\mathbf{i}},
 \end{aligned} \tag{2.8a}$$

$$\begin{aligned}
 A_1 &= \sqrt{\frac{1}{\epsilon}}, & A_2 &= \sqrt{\frac{1}{\epsilon}} \cdot \frac{-\bar{l}\bar{m} + \bar{n}\bar{\lambda}_{l,m,n}\mathbf{i}}{(\bar{m})^2 + (\bar{n})^2}, & A_3 &= \sqrt{\frac{1}{\epsilon}} \cdot \frac{-\bar{l}\bar{n} - \bar{m}\bar{\lambda}_{l,m,n}\mathbf{i}}{(\bar{m})^2 + (\bar{n})^2}, \\
 B_1 &= -\sqrt{\frac{1}{\mu}}, & B_2 &= -\sqrt{\frac{1}{\mu}} \cdot \frac{-\bar{l}\bar{m} + \bar{n}\bar{\lambda}_{l,m,n}\mathbf{i}}{(\bar{m})^2 + (\bar{n})^2}, & B_3 &= -\sqrt{\frac{1}{\mu}} \cdot \frac{-\bar{l}\bar{n} - \bar{m}\bar{\lambda}_{l,m,n}\mathbf{i}}{(\bar{m})^2 + (\bar{n})^2}, \\
 \lambda &= -\sqrt{\frac{1}{\mu\epsilon} ((\bar{l})^2 + (\bar{m})^2 + (\bar{n})^2)\mathbf{i}},
 \end{aligned} \tag{2.8b}$$

$$\begin{aligned}
 A_1 &= \sqrt{\frac{1}{\epsilon}}, & A_2 &= \sqrt{\frac{1}{\epsilon}} \cdot \frac{-\bar{l}\bar{m} - \bar{n}\bar{\lambda}_{l,m,n}\mathbf{i}}{(\bar{m})^2 + (\bar{n})^2}, & A_3 &= \sqrt{\frac{1}{\epsilon}} \cdot \frac{-\bar{l}\bar{n} + \bar{m}\bar{\lambda}_{l,m,n}\mathbf{i}}{(\bar{m})^2 + (\bar{n})^2}, \\
 B_1 &= \sqrt{\frac{1}{\mu}}, & B_2 &= \sqrt{\frac{1}{\mu}} \cdot \frac{-\bar{l}\bar{m} - \bar{n}\bar{\lambda}_{l,m,n}\mathbf{i}}{(\bar{m})^2 + (\bar{n})^2}, & B_3 &= \sqrt{\frac{1}{\mu}} \cdot \frac{-\bar{l}\bar{n} + \bar{m}\bar{\lambda}_{l,m,n}\mathbf{i}}{(\bar{m})^2 + (\bar{n})^2}, \\
 \lambda &= -\sqrt{\frac{1}{\mu\epsilon} ((\bar{l})^2 + (\bar{m})^2 + (\bar{n})^2)\mathbf{i}},
 \end{aligned} \tag{2.8c}$$

$$\begin{aligned}
 A_1 &= \sqrt{\frac{1}{\epsilon}}, & A_2 &= \sqrt{\frac{1}{\epsilon}} \cdot \frac{-\bar{l}\bar{m} - \bar{n}\bar{\lambda}_{l,m,n}\mathbf{i}}{(\bar{m})^2 + (\bar{n})^2}, & A_3 &= \sqrt{\frac{1}{\epsilon}} \cdot \frac{-\bar{l}\bar{n} + \bar{m}\bar{\lambda}_{l,m,n}\mathbf{i}}{(\bar{m})^2 + (\bar{n})^2}, \\
 B_1 &= -\sqrt{\frac{1}{\mu}}, & B_2 &= -\sqrt{\frac{1}{\mu}} \cdot \frac{-\bar{l}\bar{m} - \bar{n}\bar{\lambda}_{l,m,n}\mathbf{i}}{(\bar{m})^2 + (\bar{n})^2}, & B_3 &= -\sqrt{\frac{1}{\mu}} \cdot \frac{-\bar{l}\bar{n} + \bar{m}\bar{\lambda}_{l,m,n}\mathbf{i}}{(\bar{m})^2 + (\bar{n})^2}, \\
 \lambda &= \sqrt{\frac{1}{\mu\epsilon} ((\bar{l})^2 + (\bar{m})^2 + (\bar{n})^2)}\mathbf{i}.
 \end{aligned}
 \tag{2.8d}$$

In other words, all the eigenvalues are purely imaginary, and the corresponding eigenfunctions take the form of (2.5) if a perfectly conducting boundary is considered. This property assures the well-posedness of the PDE system (2.1) and makes the design and derivation of an efficient fourth order numerical scheme possible.

### 3. The Fourth Order Numerical Scheme

For simplicity of the presentation, we consider the computational domain  $\Omega = (0, 1)^3$  with a uniform mesh  $\Delta x = \Delta y = \Delta z = h$ . The case of different mesh sizes can be dealt with in the same fashion and does not add any mathematical difficulty.

A staggered grid was introduced and utilized in Yee’s pioneering work [22] for the Maxwell equations formulated in (2.1)–(2.2). With the node distribution of electric and magnetic field components, the first order curl operators are discretized by central differences in both time and space. The electric vector  $\mathbf{E} = (E_x, E_y, E_z)^T$  is evaluated at the mesh points  $(i \pm 1/2, j, k)$ ,  $(i, j \pm 1/2, k)$ ,  $(i, j, k \pm 1/2)$ , respectively. The magnetic vector  $\mathbf{H} = (H_x, H_y, H_z)^T$  is evaluated at the mesh points  $(i, j \pm 1/2, k \pm 1/2)$ ,  $(i \pm 1/2, j, k \pm 1/2)$ ,  $(i \pm 1/2, j \pm 1/2, k)$ , respectively. More precisely,  $E_x$  is located at the plus points,  $E_y$  at the minus points, and  $E_z$  at the cross points;  $H_x$  is located at the triangle points,  $H_y$  at the circle points, and  $H_z$  at the star points. This staggered grid is also known as the 3-D marker and cell (MAC) grid, whose 2-D version was first proposed by Harlow and Welch in [5] to deal with the numerical solution of the Navier–Stokes equations. Its advantage is the divergence-free property of the computed electric and magnetic vectors at the discrete level. See a more detailed discussion in Sec. 3.3. Note that the divergences of the electric field  $\mathbf{E}$  and the magnetic field  $\mathbf{H}$  are evaluated at  $(i, j, k)$ ,  $(i \pm 1/2, j \pm 1/2, k \pm 1/2)$ , respectively. In addition, such a choice of mesh locations for  $\mathbf{E}$  and  $\mathbf{H}$  facilitates the implementation of boundary condition (2.2).

The classical Yee scheme has been widely applied in many application problems and its capabilities have been well established. Unfortunately, a central difference approximation introduces numerical dispersion, therefore accumulating phase errors as time grows large. A fourth order numerical scheme has an obvious advantage over the standard second order centered difference scheme, because of the enormous scale of the three-dimensional setting. However, the difficulty of numerical stability (especially near the boundary) may lead to a numerical artifact, as shown in many

earlier articles. Furthermore, the efficiency of the numerical implementation of a fourth order method has always been another challenging issue.

In this article, the spatial derivatives of each variable are approximated with fourth order accuracy by long stencil differences, with the “ghost” point values recovered by one-sided extrapolation near the boundary. Such an extrapolation is accomplished by using information from the original PDE, to reduce the number of interior points needed in the one-sided formula for improved stability.

Before the formal discussion of the scheme, we introduce some finite difference and average operators to simplify the explanations below. The following notations of centered differences using different stencils at different grid points are introduced to facilitate the description:

$$D_x g(x) = \frac{g(x + \frac{1}{2}\Delta x) - g(x - \frac{1}{2}\Delta x)}{\Delta x}, \quad \tilde{D}_x g(x) = \frac{g(x + \Delta x) - g(x - \Delta x)}{2\Delta x}, \tag{3.1}$$

$$D_x^2 g(x) = \frac{g(x - \Delta x) - 2g(x) + g(x + \Delta x)}{\Delta x^2},$$

$$\begin{aligned} \mathcal{D}_x g(x) &= D_x \left( 1 - \frac{\Delta x^2}{24} D_x^2 \right) g(x) \\ &= \frac{g(x - \frac{3}{2}h) - 27g(x - \frac{1}{2}h) + 27g(x + \frac{1}{2}h) - g(x + \frac{3}{2}h)}{24\Delta x}. \end{aligned} \tag{3.2}$$

It can be easily verified by a careful Taylor expansion that the long-stencil operator in (3.2) is a fourth order approximations to  $\partial_x$ . Note that (3.2) is evaluated for variables located within a staggered grid. The corresponding operator in the  $y$ - and  $z$ -directions can be defined in a similar way. We omit the details here.

### 3.1. Update of the dynamic equations: method of lines

Due to the staggered locations of different physical variables, the components of  $\mathbf{E} = (E_x, E_y, E_z)^T$  and  $\mathbf{H} = (H_x, H_y, H_z)^T$  are updated at the “plus”, “minus”, “cross”, “triangle”, “circle” and “star” points indicated by Fig. 1, respectively. At these mesh points, the long-stencil centered difference approximation (3.2) is utilized to compute the curl of  $\mathbf{H}$  and  $\mathbf{E}$ , with fourth order accuracy. For instance, at  $(i + 1/2, j, k)$  where  $E_x$  is located, we have

$$\begin{aligned} (\mathcal{D}_y H_z)_{i+1/2,j,k} &= \frac{(H_z)_{i+1/2,j-3/2,k} - 27(H_z)_{i+1/2,j-1/2,k} + 27(H_z)_{i+1/2,j+1/2,k} - (H_z)_{i+1/2,j+3/2,k}}{24\Delta y}, \\ (\mathcal{D}_z H_y)_{i+1/2,j,k} &= \frac{(H_y)_{i+1/2,j,k-3/2} - 27(H_y)_{i+1/2,j,k-1/2} + 27(H_y)_{i+1/2,j,k+1/2} - (H_y)_{i+1/2,j,k+3/2}}{24\Delta z}, \end{aligned} \tag{3.3a}$$

and the method of lines gives

$$\partial_t E_x = \frac{1}{\epsilon} (\mathcal{D}_y H_z - \mathcal{D}_z H_y), \quad \text{at } (i + 1/2, j, k). \tag{3.3b}$$

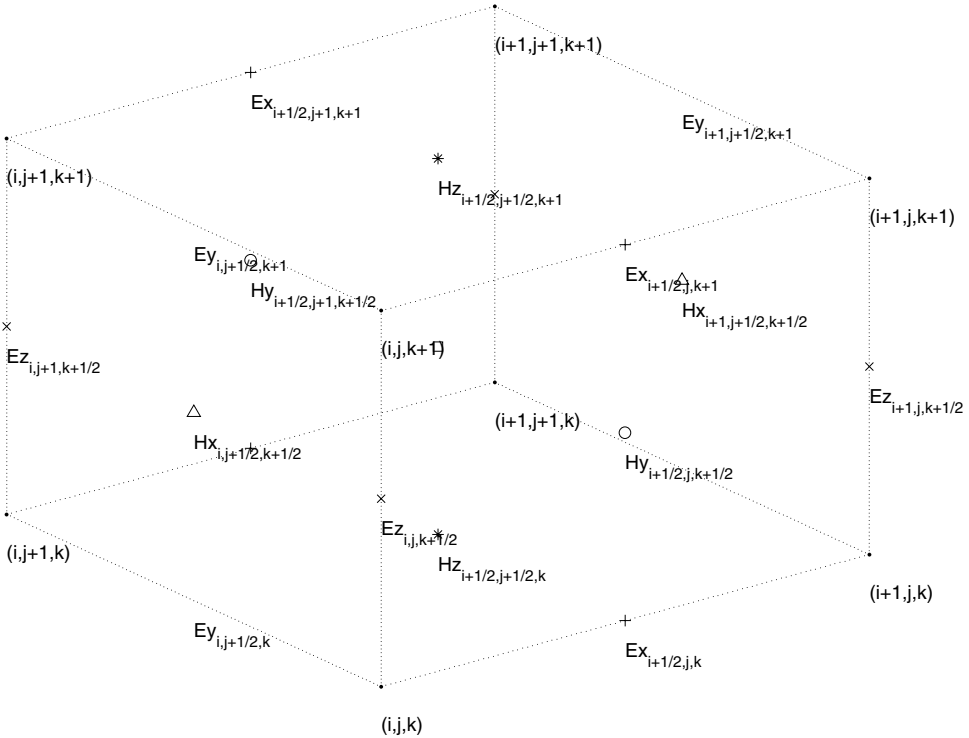


Fig. 1. The 3-D MAC grid for the Maxwell equations.

The other five components can be updated in a similar manner

$$\begin{aligned}
 \partial_t E_y &= \frac{1}{\epsilon} (\mathcal{D}_z H_x - \mathcal{D}_x H_z), & \text{at } (i, j + 1/2, k), \\
 \partial_t E_z &= \frac{1}{\epsilon} (\mathcal{D}_x H_y - \mathcal{D}_y H_x), & \text{at } (i, j, k + 1/2), \\
 \partial_t H_x &= -\frac{1}{\mu} (\mathcal{D}_y E_z - \mathcal{D}_z E_y), & \text{at } (i, j + 1/2, k + 1/2), \\
 \partial_t H_y &= -\frac{1}{\mu} (\mathcal{D}_z E_x - \mathcal{D}_x E_z), & \text{at } (i + 1/2, j, k + 1/2), \\
 \partial_t H_z &= -\frac{1}{\mu} (\mathcal{D}_x E_y - \mathcal{D}_y E_x), & \text{at } (i + 1/2, j + 1/2, k).
 \end{aligned}
 \tag{3.4}$$

### 3.2. Boundary condition and boundary extrapolation for $\mathbf{E}$ and $\mathbf{H}$

We see that the long-stencil scheme (3.3)–(3.4) requires “ghost” point values for  $\mathbf{E}$  and  $\mathbf{H}$  at a mesh point close to the boundary. For instance, since a Dirichlet boundary condition is imposed for  $E_x$  in both the  $y$ - and  $z$ -directions, we

have  $(E_x)_{i+1/2,j,0} = (E_x)_{i+1/2,j,N} = 0$  and  $(E_x)_{i+1/2,0,k} = (E_x)_{i+1/2,N,k} = 0$  on the boundary sections  $z = 0, z = 1, y = 0, y = 1$ , respectively. In turn,  $E_x$  is updated at mesh points  $(i + 1/2, j, k), 0 \leq i \leq N - 1, 1 \leq j, k \leq N - 1$ , requiring the prescription of the “ghost” values:  $(E_x)_{i+1/2,j,-1}, (E_x)_{i+1/2,j,N+1}, (E_x)_{i+1/2,-1,k}, (E_x)_{i+1/2,N+1,k}$ , due to the stencil of the discretization (3.3).

Regarding  $H_x$ , a Dirichlet boundary condition imposed in the  $x$ -direction shows that  $(H_x)_{0,j+1/2,k+1/2} = (H_x)_{N,j+1/2,k+1/2} = 0$  on the boundary sections  $x = 0, 1$ . Consequently, it is updated at mesh points  $(i, j + 1/2, k + 1/2)$  with  $1 \leq i \leq N - 1, 0 \leq j, k \leq N - 1$ . Due to the Neumann boundary condition imposed in the  $y$ - and  $z$ -directions,  $H_x$  on the boundary sections  $y = 0, 1, z = 0, 1$  is not known explicitly, only its normal derivative. It is necessary to determine “ghost” point values for  $(H_x)_{i,-1/2,k+1/2}, (H_x)_{i,-3/2,k+1/2}, (H_x)_{i,N+1/2,k+1/2}, (H_x)_{i,N+3/2,k+1/2}, (H_x)_{i,j+1/2,-1/2}, (H_x)_{i,j+1/2,-3/2}, (H_x)_{i,j+1/2,N+1/2}$  and  $(H_x)_{i,j+1/2,N+3/2}$  around the corresponding boundary sections.

The other four components can be dealt with in the same manner. Then we get

$E_x$  : updated at  $(i + 1/2, j, k), 0 \leq i \leq N - 1, 1 \leq j, k \leq N - 1$ ,

$$\begin{aligned} (E_x)_{i+1/2,j,0} = (E_x)_{i+1/2,j,N} = 0, (E_x)_{i+1/2,0,k} = (E_x)_{i+1/2,N,k} = 0, \\ (E_x)_{i+1/2,j,-1}, (E_x)_{i+1/2,j,N+1}, (E_x)_{i+1/2,-1,k}, \\ (E_x)_{i+1/2,N+1,k} \quad \text{are needed,} \end{aligned} \tag{3.5a}$$

$E_y$  : updated at  $(i, j + 1/2, k), 0 \leq j \leq N - 1, 1 \leq i, k \leq N - 1$ ,

$$\begin{aligned} (E_y)_{i,j+1/2,0} = (E_y)_{i,j+1/2,N} = 0, (E_y)_{0,j+1/2,k} = (E_y)_{N,j+1/2,k} = 0, \\ (E_y)_{i,j+1/2,-1}, (E_y)_{i,j+1/2,N+1}, (E_y)_{-1,j+1/2,k}, \\ (E_y)_{N+1,j+1/2,k} \quad \text{are needed,} \end{aligned} \tag{3.5b}$$

$E_z$  : updated at  $(i, j, k + 1/2), 0 \leq k \leq N - 1, 1 \leq i, j \leq N - 1$ ,

$$\begin{aligned} (E_z)_{i,0,k+1/2} = (E_z)_{i,N,k+1/2} = 0, (E_z)_{0,j,k+1/2} = (E_z)_{N,j,k+1/2} = 0, \\ (E_z)_{i,-1,k+1/2}, (E_z)_{i,N+1,k+1/2}, (E_z)_{-1,j,k+1/2}, \\ (E_z)_{N+1,j,k+1/2} \quad \text{are needed,} \end{aligned} \tag{3.5c}$$

$H_x$  : updated at  $(i, j + 1/2, k + 1/2), 1 \leq i \leq N - 1, 0 \leq j, k \leq N - 1$ ,

$$\begin{aligned} (H_x)_{0,j+1/2,k+1/2} = (H_x)_{N,j+1/2,k+1/2} = 0, \\ (H_x)_{i,-1/2,k+1/2}, (H_x)_{i,-3/2,k+1/2}, \\ (H_x)_{i,N+1/2,k+1/2}, (H_x)_{i,N+3/2,k+1/2}, \\ (H_x)_{i,j+1/2,-1/2}, (H_x)_{i,j+1/2,-3/2}, \\ (H_x)_{i,j+1/2,N+1/2}, (H_x)_{i,j+1/2,N+3/2} \quad \text{are needed,} \end{aligned} \tag{3.5d}$$

$H_y$  : updated at  $(i + 1/2, j, k + 1/2)$ ,  $1 \leq j \leq N - 1, 0 \leq i, k \leq N - 1$ ,

$$\begin{aligned} (H_y)_{i+1/2,0,k+1/2} &= (H_y)_{i+1/2,N,k+1/2} = 0, \\ (H_y)_{-1/2,j,k+1/2}, (H_y)_{-3/2,j,k+1/2}, \\ (H_y)_{N+1/2,j,k+1/2}, (H_y)_{N+3/2,j,k+1/2}, \\ (H_y)_{i+1/2,j,-1/2}, (H_y)_{i+1/2,j,-3/2}, \\ (H_y)_{i+1/2,j,N+1/2}, (H_y)_{i+1/2,j,N+3/2} \end{aligned} \quad \text{are needed,} \tag{3.5e}$$

$H_z$  : updated at  $(i + 1/2, j + 1/2, k)$ ,  $1 \leq k \leq N - 1, 0 \leq i, j \leq N - 1$ ,

$$\begin{aligned} (H_z)_{i+1/2,j+1/2,0} &= (H_z)_{i+1/2,j+1/2,N} = 0, \\ (H_z)_{-1/2,j+1/2,k}, (H_z)_{-3/2,j+1/2,k}, \\ (H_z)_{N+1/2,j+1/2,k}, (H_z)_{N+3/2,j+1/2,k}, \\ (H_z)_{i+1/2,-1/2,k}, (H_z)_{i+1/2,-3/2,k}, \\ (H_z)_{i+1/2,N+1/2,k}, (H_z)_{i+1/2,N+3/2,k} \end{aligned} \quad \text{are needed.} \tag{3.5f}$$

3.2.1. “Ghost” value approximation under a Dirichlet boundary condition

For instance, around the bottom boundary  $z = 0$ , a local Taylor expansion for  $E_x$  gives

$$\begin{aligned} (E_x)_{i+1/2,j,-1} &= 2(E_x)_{i+1/2,j,0} - (E_x)_{i+1/2,j,1} + h^2 \partial_z^2 (E_x)_{i+1/2,j,0} + O(h^4) \\ &= -(E_x)_{i+1/2,j,1} + h^2 \partial_z^2 (E_x)_{i+1/2,j,0} + O(h^4), \end{aligned} \tag{3.6}$$

in which the second step comes from the Dirichlet boundary condition. The term  $\partial_z^2 E_x$  for  $k = 0$  is prescribed by considering the original PDE at the boundary. Since all six components satisfy the wave equation (2.3), we have the following evaluation for  $E_x$  at  $z = 0$ :

$$\partial_t^2 E_x|_{z=0} = \frac{1}{\mu\epsilon} (\partial_x^2 + \partial_y^2) E_x|_{z=0} + \frac{1}{\mu\epsilon} \partial_z^2 E_x|_{z=0} = \frac{1}{\mu\epsilon} \partial_z^2 E_x|_{z=0}. \tag{3.7}$$

The second equality follows from the fact that  $E_x$  is identically zero along  $z = 0$ . This in turn yields

$$\partial_z^2 E_x|_{z=0} = \frac{1}{\mu\epsilon} \partial_t^2 E_x|_{z=0} = 0, \tag{3.8}$$

where the same boundary condition is utilized in the second step. A substitution of (3.8) into (3.6) leads to

$$(E_x)_{i+1/2,j,-1} = -(E_x)_{i+1/2,j,1} + O(h^4). \tag{3.9}$$

Due to its symmetry, formula (3.9) is usually referred as a “symmetric image” formula. Although the formula appears to be second order accurate, the above derivation shows that fourth order accuracy is obtained.

Analogous formulas can be derived for other physical variables and at other boundary sections. We omit the details here.

$$\begin{aligned}
 (E_x)_{i+1/2,j,-1} &= -(E_x)_{i+1/2,j,1} + O(h^4), \\
 (E_x)_{i+1/2,j,N+1} &= -(E_x)_{i+1/2,j,N-1} + O(h^4), \\
 (E_x)_{i+1/2,-1,k} &= -(E_x)_{i+1/2,1,k} + O(h^4), \\
 (E_x)_{i+1/2,N+1,k} &= -(E_x)_{i+1/2,N-1,k} + O(h^4), \\
 (E_y)_{i,j+1/2,-1} &= -(E_y)_{i,j+1/2,1} + O(h^4), \\
 (E_y)_{i,j+1/2,N+1} &= -(E_y)_{i,j+1/2,N-1} + O(h^4), \\
 (E_y)_{-1,j+1/2,k} &= -(E_y)_{1,j+1/2,k} + O(h^4), \\
 (E_y)_{N+1,j+1/2,k} &= -(E_y)_{N-1,j+1/2,k} + O(h^4), \\
 (E_z)_{i,-1,k+1/2} &= -(E_z)_{i,1,k+1/2} + O(h^4), \\
 (E_z)_{i,N+1,k+1/2} &= -(E_z)_{i,N-1,k+1/2} + O(h^4), \\
 (E_z)_{-1,j,k+1/2} &= -(E_z)_{1,j,k+1/2} + O(h^4), \\
 (E_z)_{N+1,j,k+1/2} &= -(E_z)_{N-1,j,k+1/2} + O(h^4).
 \end{aligned} \tag{3.10}$$

### 3.2.2. “Ghost” value approximation under a Neumann boundary condition

For instance, a local Taylor expansion for  $H_x$  around the bottom boundary  $z = 0$  shows that

$$\begin{aligned}
 (H_x)_{i,j+1/2,-1/2} &= (H_x)_{i,j+1/2,1/2} - \Delta z \partial_z (H_x)_{i,j+1/2,0} \\
 &\quad - \frac{\Delta z^3}{24} \partial_z^3 (H_x)_{i,j+1/2,0} + O(h^5), \\
 (H_x)_{i,j+1/2,-3/2} &= (H_x)_{i,j+1/2,3/2} - 3\Delta z \partial_z (H_x)_{i,j+1/2,0} \\
 &\quad - \frac{9\Delta z^3}{8} \partial_z^3 (H_x)_{i,j+1/2,0} + O(h^5),
 \end{aligned} \tag{3.11}$$

in which the term  $\partial_z (H_x)_{i,j+1/2,0}$  is known to vanish because of the no-flux boundary condition. The remaining work is focused on the determination of  $\partial_z^3 H_x$  at  $k = 0$ , for which we use information from the original PDE and its derivatives. Similarly, the component  $H_x$  also satisfies the wave equations indicated by (2.3):  $\partial_t^2 H_x = \frac{1}{\mu\epsilon} (\partial_x^2 + \partial_y^2 + \partial_z^2) H_x$ . Applying the vertical derivative  $\partial_z$  to this equation leads to

$$\partial_t^2 (\partial_z H_x) = \frac{1}{\mu\epsilon} (\partial_x^2 + \partial_y^2) (\partial_z H_x) + \frac{1}{\mu\epsilon} \partial_z^3 H_x, \quad \text{at } z = 0. \tag{3.12}$$

The first term on the right-hand side vanishes because of the homogeneous no-flux boundary condition. Similarly, the left-hand side is also identically zero for the same reason. As a result, we arrive at

$$\partial_z^3 H_x = \frac{1}{\mu\epsilon} \partial_t^2 (\partial_z H_x) = 0, \quad \text{at } z = 0, \tag{3.13}$$

which combined with (3.11) results in

$$\begin{aligned} (H_x)_{i,j+1/2,-1/2} &= (H_x)_{i,j+1/2,1/2} + O(h^5), \\ (H_x)_{i,j+1/2,-3/2} &= (H_x)_{i,j+1/2,3/2} + O(h^5). \end{aligned} \tag{3.14}$$

Analogous formulas for one-sided extrapolations of  $\mathbf{H}$  around each boundary sections can be derived in a similar way.

$$\begin{aligned} (H_x)_{i,j+1/2,-1/2} &= (H_x)_{i,j+1/2,1/2} + O(h^5), \\ (H_x)_{i,j+1/2,-3/2} &= (H_x)_{i,j+1/2,3/2} + O(h^5), \\ (H_x)_{i,-1/2,k+1/2} &= (H_x)_{i,1/2,k+1/2} + O(h^5), \\ (H_x)_{i,-3/2,k+1/2} &= (H_x)_{i,3/2,k+1/2} + O(h^5), \\ (H_y)_{i+1/2,j,-1/2} &= (H_y)_{i+1/2,j,1/2} + O(h^5), \\ (H_y)_{i+1/2,j,-3/2} &= (H_y)_{i+1/2,j,3/2} + O(h^5), \\ (H_y)_{-1/2,j,k+1/2} &= (H_y)_{1/2,j,k+1/2} + O(h^5), \\ (H_y)_{-3/2,j,k+1/2} &= (H_y)_{3/2,j,k+1/2} + O(h^5), \\ (H_z)_{i+1/2,-1/2,k} &= (H_z)_{i+1/2,1/2,k} + O(h^5), \\ (H_z)_{i+1/2,-3/2,k} &= (H_z)_{i+1/2,3/2,k} + O(h^5), \\ (H_z)_{-1/2,j+1/2,k} &= (H_z)_{1/2,j+1/2,k} + O(h^5), \\ (H_z)_{-3/2,j+1/2,k} &= (H_z)_{3/2,j+1/2,k} + O(h^5). \end{aligned} \tag{3.15}$$

**Remark 3.1.** There has been much work on the fourth order extension of the Yee scheme since Fang’s pioneering article [2], based on long stencil differences (3.3)–(3.4). See [6, 11, 13, 16] for relevant discussions. As mentioned above, the most challenging difficulty comes from the implementation of boundary conditions. Most earlier works utilized a one-sided closure near the metallic boundaries. For instance, a third-order closure takes the form of

$$\partial_t(E_z)_{i,\cdot} = \frac{1}{\epsilon} \left( \frac{-23(H_y)_{i-1/2,\cdot} + 21(H_y)_{i+1/2,\cdot} + 3(H_y)_{i+3/2,\cdot} - (H_y)_{i+5/2,\cdot}}{24\Delta x} - \mathcal{D}_y H_x \right), \tag{3.16}$$

at  $(i, j, k + 1/2)$ ,

for  $i$  close to 0. A fourth order closure was derived in Petropoulos and Yefet [12]. Unfortunately, such a formula breaks the symmetry around the boundary and makes a mathematical analysis impossible for the numerical curl operator, especially its discrete eigenvalue and eigenfunctions.

By contrast, formulas (3.10) and (3.15) result in a complete set of eigenvalues on the purely imaginary axis and eigenfunctions analogous to the continuous case, due to its symmetry. The details will be given in Sec. 3.4.

**Remark 3.2.** Other than long stencil differences (3.3)–(3.4), a number of alternate developments of fourth order numerical scheme can also be found in earlier references. For instance, a compact difference approximation for the spatial derivatives over the Yee stencil was utilized in [26]. This method avoids a one-sided formula so that the boundary condition can be satisfied exactly. Therefore, many promising results were presented in the numerical simulations. However, its implementation becomes complicated since the compact operator is implicit. More specifically, the determination of a derivative at any mesh point is globally connected to the derivatives at other points in the domain, which results in a tri-diagonal linear system. Some relevant discussions are also available in [9, 15, 17, 18], etc.

**Remark 3.3.** In fact, the “symmetric image” formulas (3.10) and (3.15) have even higher order accuracy. For instance, applying the wave equation for  $E_x$  on the boundary sections  $z = 0$  and  $x = 0$  repeatedly, in a similar manner as those of (3.7) and (3.12), we arrive at the estimates of  $(\partial_z^4 E_x)|_{z=0}$  and  $(\partial_x^5 E_x)|_{x=0}$

$$\begin{aligned} \partial_t^4 E_x|_{z=0} &= \frac{1}{\mu\epsilon} (\partial_x^2 + \partial_y^2) \partial_z^2 E_x|_{z=0} + \frac{1}{\mu\epsilon} \partial_z^4 E_x|_{z=0}, \\ &\text{which implies } \partial_z^4 E_x|_{z=0} = 0, \\ \partial_t^4 (\partial_x E_x)|_{x=0} &= \frac{1}{\mu\epsilon} (\partial_y^2 + \partial_z^2) (\partial_x E_x)|_{x=0} + \frac{1}{\mu\epsilon} \partial_x^5 E_x|_{x=0}, \\ &\text{which implies } \partial_x^5 E_x|_{x=0} = 0. \end{aligned} \tag{3.17}$$

Consequently, its substitution into a sixth order Taylor expansion for  $E_x$  around the boundary sections  $z = 0$  and  $x = 0$  gives

$$\begin{aligned} (E_x)_{i+1/2,j,-1} &= 2(E_x)_{i+1/2,j,0} - (E_x)_{i+1/2,j,1} + \Delta x^2 \partial_z^2 (E_x)_{i+1/2,j,0} \\ &\quad + \frac{\Delta x^4}{12} \partial_z^4 (E_x)_{i+1/2,j,0} + O(h^6) \\ &= -(E_x)_{i+1/2,j,1} + \frac{\Delta x^4}{12} \partial_z^4 (E_x)_{i+1/2,j,0} + O(h^6) \\ &= -(E_x)_{i+1/2,j,1} + O(h^6), \\ (E_x)_{-1/2,j,k} &= (E_x)_{1/2,j,k} - \frac{\Delta x^3}{24} \partial_x^3 (E_x)_{0,j,k} - \frac{\Delta x^5}{1920} \partial_x^5 (E_x)_{0,j,k} + O(h^7) \\ &= (E_x)_{1/2,j,k} - \frac{\Delta x^5}{1920} \partial_x^5 (E_x)_{0,j,k} + O(h^7) = (E_x)_{1/2,j,k} + O(h^7). \end{aligned} \tag{3.18}$$

Similar derivations can be applied for other physical variables at other boundary sections. Therefore, extrapolation formulas (3.10) and (3.15) result in sixth order accuracy around the boundary.

**Remark 3.4.** The idea of a symmetric boundary extrapolation formula was also discussed in the second author’s earlier works [10, 14, 19], in which fourth order finite difference schemes for incompressible fluid were proposed and analyzed. In the fluid model, such a symmetric formula works well and gives very accurate numerical results. A theoretical analysis of the symmetric formula for the dissipative fluid system was also provided. For the Maxwell equations, this technique can be applied in a similar way. The detailed fourth order convergence analysis for the proposed scheme will be given in a forthcoming article.

**3.3. Divergence-free property for the numerical electric and magnetic vectors at a discrete level**

The divergence and curl of the electric and magnetic vectors  $\mathbf{E}$  and  $\mathbf{H}$  at the discrete level are defined as

$$\begin{aligned}
 \nabla_h \cdot \mathbf{E} &= \mathcal{D}_x E_x + \mathcal{D}_y E_y + \mathcal{D}_z E_z, \quad \text{at } (i, j, k), \\
 \nabla_h \cdot \mathbf{H} &= \mathcal{D}_x H_x + \mathcal{D}_y H_y + \mathcal{D}_z H_z, \quad \text{at } (i + 1/2, j + 1/2, k + 1/2), \\
 \nabla_h \times \mathbf{E} &= \begin{pmatrix} (\mathcal{D}_y E_z - \mathcal{D}_z E_y)_{i, j+1/2, k+1/2} \\ (\mathcal{D}_z E_x - \mathcal{D}_x E_z)_{i+1/2, j, k+1/2} \\ (\mathcal{D}_x E_y - \mathcal{D}_y E_x)_{i+1/2, j+1/2, k} \end{pmatrix}, \\
 \nabla_h \times \mathbf{H} &= \begin{pmatrix} (\mathcal{D}_y H_z - \mathcal{D}_z H_y)_{i+1/2, j, k} \\ (\mathcal{D}_z H_x - \mathcal{D}_x H_z)_{i, j+1/2, k} \\ (\mathcal{D}_x H_y - \mathcal{D}_y H_x)_{i, j, k+1/2} \end{pmatrix}.
 \end{aligned} \tag{3.19}$$

Note that all these quantities represent a fourth order numerical approximation to the exact values. It is clear that the components of curl of  $\mathbf{E}$  are located at the same mesh points as those of  $\mathbf{H}$ , while the components of curl of  $\mathbf{H}$  are located at the same mesh points as those of  $\mathbf{E}$ . This fact drastically facilitates the time marching effort in the Maxwell equations, as will be shown later. Meanwhile, since the coordinate system is orthogonal, we observe that the composition of the divergence and curl operator results in an identically zero value for both  $\mathbf{E}$  and  $\mathbf{H}$ , at the discrete level:

$$\begin{aligned}
 \nabla_h \cdot (\nabla_h \times \mathbf{H}) &= \mathcal{D}_x (\mathcal{D}_y H_z - \mathcal{D}_z H_y) + \mathcal{D}_y (\mathcal{D}_z H_x - \mathcal{D}_x H_z) \\
 &\quad + \mathcal{D}_z (\mathcal{D}_x H_y - \mathcal{D}_y H_x) \\
 &= 0, \quad \text{at } (i, j, k), \\
 \nabla_h \cdot (\nabla_h \times \mathbf{E}) &= \mathcal{D}_x (\mathcal{D}_y E_z - \mathcal{D}_z E_y) + \mathcal{D}_y (\mathcal{D}_z E_x - \mathcal{D}_x E_z) \\
 &\quad + \mathcal{D}_z (\mathcal{D}_x E_y - \mathcal{D}_y E_x) \\
 &= 0, \quad \text{at } (i + 1/2, j + 1/2, k + 1/2).
 \end{aligned} \tag{3.20}$$

As a result, the scheme of method of lines (3.3)-(3.4) indicates

$$\begin{aligned} \partial_t (\nabla_h \cdot \mathbf{E}) &= \frac{1}{\epsilon} \nabla_h \cdot (\nabla_h \times \mathbf{H}) = 0, \quad \text{at } (i, j, k), \\ \partial_t (\nabla_h \cdot \mathbf{H}) &= -\frac{1}{\mu} \nabla_h \cdot (\nabla_h \times \mathbf{E}) = 0, \quad \text{at } (i + 1/2, j + 1/2, k + 1/2), \end{aligned} \tag{3.21}$$

which comes from the fact that all the spatial operators are commutative. In other words, both  $\mathbf{E}$  and  $\mathbf{H}$  remain divergence-free (at the discrete level with a fourth order numerical approximation) if the initial data  $\mathbf{E}(\cdot, t = 0)$  and  $\mathbf{H}(\cdot, t = 0)$  have zero divergence.

### 3.4. Eigenfunctions and eigenvalues of the discrete curl operator

One prominent advantage of the proposed fourth order scheme on the staggered grid can be seen from the complete set of eigenfunctions and eigenvalues of the curl operator at the discrete level. Because of the symmetric boundary extrapolation formulas (3.10) and (3.15), the components of  $\mathbf{E}$  and  $\mathbf{H}$  can be represented as

$$\begin{aligned} (E_x)_{i+1/2,j,k} &= \sum_{l=0}^{N-1} \sum_{m=0}^{N-1} \sum_{n=0}^{N-1} A_{1m,n,k} \\ &\quad \times \cos\left(\frac{l(i+1/2)\pi}{N}\right) \sin\left(\frac{mj\pi}{N}\right) \sin\left(\frac{nk\pi}{N}\right), \\ (E_y)_{i,j+1/2,k} &= \sum_{l=0}^{N-1} \sum_{m=0}^{N-1} \sum_{n=0}^{N-1} A_{2m,n,k} \\ &\quad \times \sin\left(\frac{li\pi}{N}\right) \cos\left(\frac{m(j+1/2)\pi}{N}\right) \sin\left(\frac{nk\pi}{N}\right), \\ (E_z)_{i,j,k+1/2} &= \sum_{l=0}^{N-1} \sum_{m=0}^{N-1} \sum_{n=0}^{N-1} A_{3m,n,k} \\ &\quad \times \sin\left(\frac{li\pi}{N}\right) \sin\left(\frac{mj\pi}{N}\right) \cos\left(\frac{n(k+1/2)\pi}{N}\right), \\ (H_x)_{i,j+1/2,k+1/2} &= \sum_{l=0}^{N-1} \sum_{m=0}^{N-1} \sum_{n=0}^{N-1} B_{1m,n,k} \\ &\quad \times \sin\left(\frac{li\pi}{N}\right) \cos\left(\frac{m(j+1/2)\pi}{N}\right) \cos\left(\frac{n(k+1/2)\pi}{N}\right), \\ (H_y)_{i+1/2,j,k+1/2} &= \sum_{l=0}^{N-1} \sum_{m=0}^{N-1} \sum_{n=0}^{N-1} B_{2m,n,k} \\ &\quad \times \cos\left(\frac{l(i+1/2)\pi}{N}\right) \sin\left(\frac{mj\pi}{N}\right) \cos\left(\frac{n(k+1/2)\pi}{N}\right), \end{aligned}$$

$$\begin{aligned}
 (H_z)_{i+1/2,j+1/2,k} &= \sum_{l=0}^{N-1} \sum_{m=0}^{N-1} \sum_{n=0}^{N-1} B_{3m,n,k} \\
 &\quad \times \cos\left(\frac{l(i+1/2)\pi}{N}\right) \cos\left(\frac{m(j+1/2)\pi}{N}\right) \sin\left(\frac{nk\pi}{N}\right).
 \end{aligned} \tag{3.22}$$

For simplicity of description, we look at the profile of  $\mathbf{E}$  and  $\mathbf{H}$  with a single mode  $(l, m, n)$ :

$$\begin{aligned}
 (E_x)_{i+1/2,j,k} &= A_1 \cos\left(\frac{l(i+1/2)\pi}{N}\right) \sin\left(\frac{mj\pi}{N}\right) \sin\left(\frac{nk\pi}{N}\right), \\
 (E_y)_{i,j+1/2,k} &= A_2 \sin\left(\frac{li\pi}{N}\right) \cos\left(\frac{m(j+1/2)\pi}{N}\right) \sin\left(\frac{nk\pi}{N}\right), \\
 (E_z)_{i,j,k+1/2} &= A_3 \sin\left(\frac{li\pi}{N}\right) \sin\left(\frac{mj\pi}{N}\right) \cos\left(\frac{n(k+1/2)\pi}{N}\right), \\
 (H_x)_{i,j+1/2,k+1/2} &= B_1 \sin\left(\frac{li\pi}{N}\right) \cos\left(\frac{m(j+1/2)\pi}{N}\right) \cos\left(\frac{n(k+1/2)\pi}{N}\right), \\
 (H_y)_{i+1/2,j,k+1/2} &= B_2 \cos\left(\frac{l(i+1/2)\pi}{N}\right) \sin\left(\frac{mj\pi}{N}\right) \cos\left(\frac{n(k+1/2)\pi}{N}\right), \\
 (H_z)_{i+1/2,j+1/2,k} &= B_3 \cos\left(\frac{l(i+1/2)\pi}{N}\right) \cos\left(\frac{m(j+1/2)\pi}{N}\right) \sin\left(\frac{nk\pi}{N}\right).
 \end{aligned} \tag{3.23}$$

An application of the long stencil difference to these profiles leads to the following results:

$$\begin{aligned}
 (\mathcal{D}_x E_x)_{i,j,k} &= -A_1 \bar{l}' \sin\left(\frac{li\pi}{N}\right) \sin\left(\frac{mj\pi}{N}\right) \sin\left(\frac{nk\pi}{N}\right), \\
 (\mathcal{D}_y E_x)_{i+1/2,j+1/2,k} &= A_1 \bar{m}' \cos\left(\frac{l(i+1/2)\pi}{N}\right) \\
 &\quad \times \cos\left(\frac{m(j+1/2)\pi}{N}\right) \sin\left(\frac{nk\pi}{N}\right), \\
 (\mathcal{D}_z E_x)_{i+1/2,j,k+1/2} &= A_1 \bar{n}' \cos\left(\frac{l(i+1/2)\pi}{N}\right) \\
 &\quad \times \sin\left(\frac{mj\pi}{N}\right) \cos\left(\frac{n(k+1/2)\pi}{N}\right),
 \end{aligned} \tag{3.24a}$$

with

$$\begin{aligned} \bar{l}' &= \frac{\sin(l\pi\Delta x)}{\Delta x} \left[ 1 + \frac{\Delta x^2}{3} \sin^2\left(\frac{l\pi\Delta x}{2}\right) \right], \\ \bar{m}' &= \frac{\sin(m\pi\Delta y)}{\Delta y} \left[ 1 + \frac{\Delta y^2}{3} \sin^2\left(\frac{m\pi\Delta y}{2}\right) \right], \\ \bar{n}' &= \frac{\sin(n\pi\Delta z)}{\Delta z} \left[ 1 + \frac{\Delta z^2}{3} \sin^2\left(\frac{n\pi\Delta z}{2}\right) \right]. \end{aligned} \tag{3.24b}$$

Similarly, we have

$$\begin{aligned} (\mathcal{D}_x E_y)_{i+1/2, j+1/2, k} &= A_2 \bar{l}' \cos\left(\frac{l(i+1/2)\pi}{N}\right) \\ &\quad \times \cos\left(\frac{m(j+1/2)\pi}{N}\right) \sin\left(\frac{nk\pi}{N}\right), \\ (\mathcal{D}_y E_y)_{i, j, k} &= -A_2 \bar{m}' \sin\left(\frac{li\pi}{N}\right) \sin\left(\frac{mj\pi}{N}\right) \sin\left(\frac{nk\pi}{N}\right), \end{aligned} \tag{3.25a}$$

$$\begin{aligned} (\mathcal{D}_z E_y)_{i, j+1/2, k+1/2} &= A_2 \bar{n}' \sin\left(\frac{li\pi}{N}\right) \\ &\quad \times \cos\left(\frac{m(j+1/2)\pi}{N}\right) \cos\left(\frac{n(k+1/2)\pi}{N}\right), \end{aligned}$$

$$\begin{aligned} (\mathcal{D}_x E_z)_{i+1/2, j, k+1/2} &= A_3 \bar{l}' \cos\left(\frac{l(i+1/2)\pi}{N}\right) \\ &\quad \times \sin\left(\frac{mj\pi}{N}\right) \cos\left(\frac{n(k+1/2)\pi}{N}\right), \\ (\mathcal{D}_y E_z)_{i, j+1/2, k+1/2} &= A_3 \bar{m}' \sin\left(\frac{li\pi}{N}\right) \end{aligned} \tag{3.25b}$$

$$\times \cos\left(\frac{m(j+1/2)\pi}{N}\right) \cos\left(\frac{n(k+1/2)\pi}{N}\right),$$

$$(\mathcal{D}_z E_z)_{i, j, k} = -A_3 \bar{n}' \sin\left(\frac{li\pi}{N}\right) \sin\left(\frac{mj\pi}{N}\right) \sin\left(\frac{nk\pi}{N}\right),$$

$$\begin{aligned} (\mathcal{D}_x H_x)_{i+1/2, j+1/2, k+1/2} &= B_1 \bar{l}' \cos\left(\frac{l(i+1/2)\pi}{N}\right) \\ &\quad \times \cos\left(\frac{m(j+1/2)\pi}{N}\right) \cos\left(\frac{n(k+1/2)\pi}{N}\right), \end{aligned}$$

$$\begin{aligned}
(\mathcal{D}_y H_x)_{i,j+1/2,k+1/2} &= -B_1 \bar{m}' \sin\left(\frac{li\pi}{N}\right) \\
&\quad \times \sin\left(\frac{mj\pi}{N}\right) \cos\left(\frac{n(k+1/2)\pi}{N}\right), \\
(\mathcal{D}_z H_x)_{i,j+1/2,k+1/2} &= -B_1 \bar{n}' \sin\left(\frac{li\pi}{N}\right) \\
&\quad \times \cos\left(\frac{m(j+1/2)\pi}{N}\right) \sin\left(\frac{nk\pi}{N}\right),
\end{aligned} \tag{3.25c}$$

$$\begin{aligned}
(\mathcal{D}_x H_y)_{i,j,k+1/2} &= -B_2 \bar{l}' \sin\left(\frac{li\pi}{N}\right) \\
&\quad \times \sin\left(\frac{mj\pi}{N}\right) \cos\left(\frac{n(k+1/2)\pi}{N}\right), \\
(\mathcal{D}_y H_y)_{i+1/2,j+1/2,k+1/2} &= B_2 \bar{m}' \cos\left(\frac{l(i+1/2)\pi}{N}\right) \\
&\quad \times \cos\left(\frac{m(j+1/2)\pi}{N}\right) \cos\left(\frac{n(k+1/2)\pi}{N}\right), \\
(\mathcal{D}_z H_y)_{i+1/2,j,k} &= -B_2 \bar{n}' \cos\left(\frac{l(i+1/2)\pi}{N}\right) \\
&\quad \times \sin\left(\frac{mj\pi}{N}\right) \sin\left(\frac{nk\pi}{N}\right),
\end{aligned} \tag{3.25d}$$

$$\begin{aligned}
(\mathcal{D}_x H_z)_{i,j+1/2,k} &= -B_3 \bar{l}' \sin\left(\frac{li\pi}{N}\right) \\
&\quad \times \cos\left(\frac{m(j+1/2)\pi}{N}\right) \sin\left(\frac{nk\pi}{N}\right), \\
(\mathcal{D}_y H_z)_{i+1/2,j,k} &= -B_3 \bar{m}' \cos\left(\frac{l(i+1/2)\pi}{N}\right) \\
&\quad \times \sin\left(\frac{mj\pi}{N}\right) \sin\left(\frac{nk\pi}{N}\right), \\
(\mathcal{D}_z H_z)_{i+1/2,j+1/2,k+1/2} &= B_3 \bar{n}' \cos\left(\frac{l(i+1/2)\pi}{N}\right) \\
&\quad \times \cos\left(\frac{m(j+1/2)\pi}{N}\right) \cos\left(\frac{n(k+1/2)\pi}{N}\right).
\end{aligned} \tag{3.25e}$$

Since the numerical vectors  $\mathbf{E}$  and  $\mathbf{H}$  are divergence-free at the discrete level as shown in Sec. 3.3, the above equations yield

$$A_1 \bar{l}' + A_2 \bar{m}' + A_3 \bar{n}' = 0, \quad B_1 \bar{l}' + B_2 \bar{m}' + B_3 \bar{n}' = 0, \quad (3.26)$$

in which  $l^*, m^*, n^*$  are given by formula (3.24b).

Next, we are going to show that all the eigenvalues of the discrete curl operator are purely imaginary and the corresponding eigenfunctions take the same form as that of (2.5). From the calculations (3.24)–(3.25), it is obvious that a single mode profile (3.23) becomes an eigenfunction if

$$\begin{aligned} -\frac{1}{\epsilon} (\bar{m}' B_3 - \bar{n}' B_2) &= \lambda A_1, & -\frac{1}{\epsilon} (\bar{n}' B_1 - \bar{l}' B_3) &= \lambda A_2, \\ -\frac{1}{\epsilon} (\bar{l}' B_2 - \bar{m}' B_1) &= \lambda A_3, & -\frac{1}{\mu} (\bar{m}' A_3 - \bar{n}' A_2) &= \lambda B_1, \\ -\frac{1}{\mu} (\bar{n}' A_1 - \bar{l}' A_3) &= \lambda B_2, & -\frac{1}{\mu} (\bar{l}' A_2 - \bar{m}' A_1) &= \lambda B_3. \end{aligned} \quad (3.27)$$

Using the same argument as that of (2.8), a complete set of eigenvalues and the corresponding coefficients are given by (with  $\bar{\lambda}'_{l,m,n} = \sqrt{(\bar{l}')^2 + (\bar{m}')^2 + (\bar{n}')^2}$ )

$$\begin{aligned} A_1 &= \sqrt{\frac{1}{\epsilon}}, & A_2 &= \sqrt{\frac{1}{\epsilon}} \cdot \frac{-\bar{l}' \bar{m}' + \bar{n}' \bar{\lambda}'_{l,m,n} \mathbf{i}}{(\bar{m}')^2 + (\bar{n}')^2}, \\ A_3 &= \sqrt{\frac{1}{\epsilon}} \cdot \frac{-\bar{l}' \bar{n}' - \bar{m}' \bar{\lambda}'_{l,m,n} \mathbf{i}}{(\bar{m}')^2 + (\bar{n}')^2}, \\ B_1 &= \pm \sqrt{\frac{1}{\mu}}, & B_2 &= \pm \sqrt{\frac{1}{\mu}} \cdot \frac{-\bar{l}' \bar{m}' + \bar{n}' \bar{\lambda}'_{l,m,n} \mathbf{i}}{(\bar{m}')^2 + (\bar{n}')^2}, \\ B_3 &= \pm \sqrt{\frac{1}{\mu}} \cdot \frac{-\bar{l}' \bar{n}' - \bar{m}' \bar{\lambda}'_{l,m,n} \mathbf{i}}{(\bar{m}')^2 + (\bar{n}')^2}, \\ \lambda &= \pm \sqrt{\frac{1}{\mu \epsilon} ((\bar{l}')^2 + (\bar{m}')^2 + (\bar{n}')^2)} \mathbf{i}, \end{aligned} \quad (3.28a)$$

$$\begin{aligned} A_1 &= \sqrt{\frac{1}{\epsilon}}, & A_2 &= \sqrt{\frac{1}{\epsilon}} \cdot \frac{-\bar{l}' \bar{m}' - \bar{n}' \bar{\lambda}'_{l,m,n} \mathbf{i}}{(\bar{m}')^2 + (\bar{n}')^2}, \\ A_3 &= \sqrt{\frac{1}{\epsilon}} \cdot \frac{-\bar{l}' \bar{n}' + \bar{m}' \bar{\lambda}'_{l,m,n} \mathbf{i}}{(\bar{m}')^2 + (\bar{n}')^2}, \\ B_1 &= \pm \sqrt{\frac{1}{\mu}}, & B_2 &= \pm \sqrt{\frac{1}{\mu}} \cdot \frac{-\bar{l}' \bar{m}' - \bar{n}' \bar{\lambda}'_{l,m,n} \mathbf{i}}{(\bar{m}')^2 + (\bar{n}')^2}, \\ B_3 &= \pm \sqrt{\frac{1}{\mu}} \cdot \frac{-\bar{l}' \bar{n}' + \bar{m}' \bar{\lambda}'_{l,m,n} \mathbf{i}}{(\bar{m}')^2 + (\bar{n}')^2}, \\ \lambda &= \mp \sqrt{\frac{1}{\mu \epsilon} ((\bar{l}')^2 + (\bar{m}')^2 + (\bar{n}')^2)} \mathbf{i}. \end{aligned} \quad (3.28b)$$

Therefore, for each integer index  $(l, m, n)$ , there are four eigenfunctions with eigenvalues  $\lambda_{l,m,n} = \pm \sqrt{\frac{1}{\mu\epsilon}} \bar{\chi}_{l,m,n} \mathbf{i}$ . In other words, the discrete curl operator created by long-stencil difference (3.2a) along with the “symmetric image” formulas (3.10), (3.15) results in a complete set of eigenvalues and eigenfunctions with the same form as the continuous case (2.8). There is only a slight modification from the continuous formulas, due to the fourth order approximations.

### 3.5. Temporal discretization

Due to the hyperbolic property of the curl operator, a fully explicit scheme must be applied. In the classical Yee scheme, the components of  $\mathbf{E}$  and  $\mathbf{H}$  are computed alternately in the leap-frog manner. Furthermore, the leap-frog integration is known to be stable under a CFL constraint

$$\sqrt{\frac{1}{\mu\epsilon}} \sqrt{\frac{1}{\Delta x^2} + \frac{1}{\Delta y^2} + \frac{1}{\Delta z^2}} \leq \frac{1}{\Delta t}. \tag{3.29}$$

Meanwhile, the leap-frog scheme turns out to be highly dispersive and thus leads to an accumulation of phase errors in late-time data analysis, due to its central difference feature. As a result, its higher order extension has attracted much attention. For instance, a fourth order leap frog method was briefly introduced in Fang [2] and subsequently discussed in Young [26]. In particular, the numerical values of a physical variable  $f$  at the time step  $t^{n+1}$  is determined from  $f$  at  $t^n$ , its first order and third order correctional temporal derivatives at  $t^{n+1/2}$ :  $f^{n+1} = f^n + \Delta t \partial_t f^{n+1/2} + \frac{\Delta t^3}{24} \partial_t^3 f^{n+1/2} + O(\Delta t^5)$ . For each variable, the first order term is given by the curl operator and the third order correctional term is converted into spatial derivatives through a repeated application of the Maxwell equations. For instance, the electric field vector is updated using

$$\mathbf{E}^{n+1} = \mathbf{E}^n + \frac{\Delta t}{\epsilon} \nabla_h \times \mathbf{H}^{n+1/2} + \frac{1}{\mu\epsilon^2} \cdot \frac{\Delta t^3}{24} \nabla_h \times (\nabla_h^2 \mathbf{H}^{n+1/2}) + O(\Delta t^5). \tag{3.30}$$

However, the implementation of boundary conditions and the computation of the curl-Laplacian term becomes very complicated, as shown in Fang’s article [2]. Therefore, this fourth order approach is not recommended in practical computation.

The four-stage Runge–Kutta (RK) integrator is considered in this article. Given the electric and magnetic field vectors  $\mathbf{E}^n$  and  $\mathbf{H}^n$  at the time step  $t^n$ , we set  $\mathbf{y}^n = (\mathbf{E}^n, \mathbf{H}^n)^T$  and denote  $\mathbf{f}(\mathbf{y}^n) = (\frac{1}{\epsilon} \nabla_h \times \mathbf{H}^n, -\frac{1}{\mu} \nabla_h \times \mathbf{E}^n)^T$ , the discrete curl operator. Note that  $\mathbf{f}$  is a linear transformation of  $\mathbf{y}^n$ . In other words, this transformation can be represented as  $\mathbf{f}(\mathbf{y}^n) = \mathbf{A} \mathbf{y}^n$ , with  $\mathbf{A}$  a constant matrix.

Classical RK4

$$\begin{aligned}
 \mathbf{y}^{n,(1)} &= \mathbf{y}^n + \frac{1}{2} \Delta t \mathbf{f}(\mathbf{y}^n), \\
 \mathbf{y}^{n,(2)} &= \mathbf{y}^n + \frac{1}{2} \Delta t \mathbf{f}(\mathbf{y}^{n,(1)}), \\
 \mathbf{y}^{n,(3)} &= \mathbf{y}^n + \Delta t \mathbf{f}(\mathbf{y}^{n,(2)}), \\
 \mathbf{y}^{n+1} &= \frac{1}{3}(-\mathbf{y}^n + \mathbf{y}^{n,(1)} + 2\mathbf{y}^{n,(2)} + \mathbf{y}^{n,(3)}) + \frac{1}{6} \Delta t \mathbf{f}(\mathbf{y}^{n,(3)}).
 \end{aligned}
 \tag{3.31}$$

The classical RK4 method gives a full fourth order accuracy in time and leads to a much improved stability criterion compared to the classical Yee scheme, as will be explained in detail later. A similar argument can be found in [26], in which the authors combined the classical RK4 with a compact difference.

Meanwhile, as mentioned in [26], the main disadvantage of the classical four-stage RK integrator is its requirement of additional memory at each time step, since the numerical values of  $\mathbf{y}^{n,(i)}$ ,  $i = 1, 2, 3$ , have to be stored at each RK stage. To overcome this disadvantage, we utilize the Jameson method, an alternate four-stage RK method, in this article. With the same notations as that of (3.31), the scheme can be written as the following.

Jameson’s method

$$\begin{aligned}
 \mathbf{y}^{n,(1)} &= \mathbf{y}^n + \frac{1}{4} \Delta t \mathbf{f}(\mathbf{y}^n), \\
 \mathbf{y}^{n,(2)} &= \mathbf{y}^n + \frac{1}{3} \Delta t \mathbf{f}(\mathbf{y}^{n,(1)}), \\
 \mathbf{y}^{n,(3)} &= \mathbf{y}^n + \frac{1}{2} \Delta t \mathbf{f}(\mathbf{y}^{n,(2)}), \\
 \mathbf{y}^{n+1} &= \mathbf{y}^n + \Delta t \mathbf{f}(\mathbf{y}^{n,(3)}).
 \end{aligned}
 \tag{3.32}$$

This multi-stage time integration was proposed by Jameson in [7,8] in the numerical simulations of gas dynamics. It is obvious that the memory storage is drastically reduced, since only the numerical profile at the previous time stage is needed in the time integration for each physical variable. Meanwhile, it should be noted that the Jameson scheme is only second order accurate for nonlinear gas dynamics. However, such a time integration gives a full fourth order accuracy for the Maxwell equations because of their linearity. In fact, since  $\mathbf{f}$  is linear, we observe that the classical RK4 method (3.31) and Jameson’s method (3.32) give exactly the same numerical value of  $\mathbf{y}$  at  $t^{n+1}$ :

$$\mathbf{y}^{n+1} = \left( I + \Delta t A + \frac{\Delta t^2}{2} A^2 + \frac{\Delta t^3}{6} A^3 + \frac{\Delta t^4}{24} A^4 \right) \mathbf{y}^n.
 \tag{3.33}$$

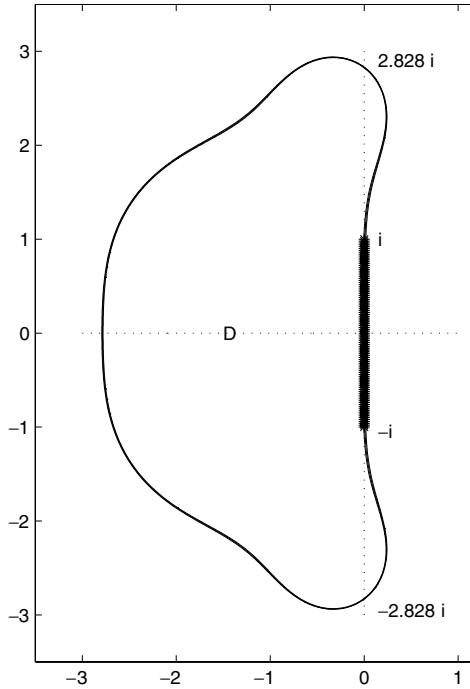


Fig. 2. Stability domain of the classical *RK4*, the Jameson method and the classical leap frog. *D* represents the common stability domain of the classical *RK4* and the Jameson method, and the bold line represents that of the leap frog.

Regarding the numerical stability in time, we see that the stability domains of the classical *RK4* and Jameson’s method are the same. Their common stability domain is shown in Fig. 2, along with that of the classical leap frog time integration.

We see that the stability domain of *RK4* and Jameson method contains a 2-D region, while that of the leap frog only contains a line segment on the purely imaginary axis:

$$D_{LF} = \left\{ z = \alpha i : -\frac{1}{\Delta t} \leq \alpha \leq \frac{1}{\Delta t} \right\}. \tag{3.34}$$

For the stability domain  $D_{RK4}$ , we see that

$$D_I = \left\{ z = \alpha i : -\frac{2\sqrt{2}}{\Delta t} \leq \alpha \leq \frac{2\sqrt{2}}{\Delta t} \right\} \subset D_{RK4}. \tag{3.35}$$

Consequently, if the all the eigenvalues of the discrete curl operator lie within  $D_I$  given by (3.35), the Jameson scheme becomes stable. Since the eigenvalues are given

by  $\lambda_{l,m,n} = \pm \sqrt{\frac{1}{\mu\epsilon} ((\bar{l}')^2 + (\bar{m}')^2 + (\bar{n}')^2)} \mathbf{i}$ , we observe that the numerical stability condition is equivalent to

$$\max_{l,m,n} \sqrt{\frac{1}{\mu\epsilon} ((\bar{l}')^2 + (\bar{m}')^2 + (\bar{n}')^2)} \leq \frac{2\sqrt{2}}{\Delta t}. \tag{3.36}$$

Meanwhile, formula (3.24b) shows that

$$\bar{l}' \leq \frac{|\sin(l\pi\Delta x)|}{\Delta x} \left[ 1 + \frac{1}{3} \sin^2\left(\frac{l\pi\Delta x}{2}\right) \right] \leq \frac{\sin(\frac{\pi}{2})}{\Delta x} \left[ 1 + \frac{1}{3} \sin^2\left(\frac{\pi}{4}\right) \right] = \frac{7}{6\Delta x}, \tag{3.37a}$$

and similar estimates in  $y$ - and  $z$ -directions can be obtained:

$$\bar{m}' \leq \frac{7}{6\Delta y}, \quad \bar{n}' \leq \frac{7}{6\Delta z}. \tag{3.37b}$$

As a result, the stability condition (3.34) is satisfied provided that

$$\sqrt{\frac{1}{\mu\epsilon} \sqrt{\frac{1}{\Delta x^2} + \frac{1}{\Delta y^2} + \frac{1}{\Delta z^2}}} \leq \frac{6}{7} \cdot \frac{2\sqrt{2}}{\Delta t} = \frac{12\sqrt{2}}{7} \cdot \frac{1}{\Delta t}. \tag{3.38}$$

In other words, the overall fourth order scheme has a maximum CFL number of  $\frac{12\sqrt{2}}{7}$ , which is a drastic improvement. Moreover, the Jameson method preserves both fourth order accuracy and the stability domain, while it drastically reduces the required memory.

**Remark 3.5.** The CFL constraint (3.29) for the classical Yee scheme can also be derived from the stability domain  $D_{LF}$  given by (3.34). Moreover, a similar analysis can be applied to a  $2 \times 4$  scheme, i.e. long stencil difference approximation coupled with leap frog time integration. The combination of the estimate (3.37) for  $\bar{l}'$ ,  $\bar{m}'$ ,  $\bar{n}'$  and the stability domain (3.34) shows that the  $2 \times 4$  scheme is conditionally stable if

$$\sqrt{\frac{1}{\mu\epsilon} \sqrt{\frac{1}{\Delta x^2} + \frac{1}{\Delta y^2} + \frac{1}{\Delta z^2}}} \leq \frac{6}{7} \cdot \frac{1}{\Delta t} = \frac{6}{7\Delta t}. \tag{3.39}$$

As a result, we see that the proposed  $4 \times 4$  scheme has a better stability property than that of the  $2 \times 2$  and  $2 \times 4$  schemes.

**Remark 3.6.** The  $\frac{6}{7}$  factor in the CFL stability condition for the fourth order long stencil approximation was first reported by Fang in [2]. This result was also cited in a relevant work [25]. Yet, the derivation was based on Von Neumann analysis, with an assumption of periodic boundary conditions for  $\mathbf{E}$  and  $\mathbf{H}$ . Our work is the first such result with perfectly conducting boundary conditions imposed for all physical variables.

**Remark 3.7.** Since the Jameson method (3.32) is fully explicit, we see that the numerical profile  $\mathbf{y}^{n,(i)}$  ( $i = 1, 2, 3$ ) is divergence-free, using the same argument

for the discrete curl operator in Sec. 3.3. As a result, a divergence-free vector  $\mathbf{y}^n = (\mathbf{E}^n, \mathbf{H}^n)^T$  leads to a numerical profile  $\mathbf{y}^{n+1} = (\mathbf{E}^{n+1}, \mathbf{H}^{n+1})^T$  with zero divergence at a discrete level. Hence, the proposed numerical scheme is proven to preserve the divergence-free property.

#### 4. Numerical Accuracy Check

In this section, we perform an accuracy check for the proposed fourth order scheme over the Yee grid. For simplicity, we set the computational domain as a cubic box  $\Omega = (0, a_1) \times (0, a_2) \times (0, a_3)$  with  $a_1 = a_2 = a_3 = 1$  and the physical parameters as  $\mu = \epsilon = 1$ . The initial data is chosen to contain a single mode with  $l = m = n = 1$ :

$$\begin{aligned} E_x(\cdot, t = 0) &= \cos(\pi x) \sin(\pi y) \sin(\pi z), & E_y(\cdot, t = 0) &= 0, \\ E_z(\cdot, t = 0) &= -\sin(\pi x) \sin(\pi y) \cos(\pi z), & & \\ H_x(\cdot, t = 0) &= 0, & H_y(\cdot, t = 0) &= 0, & H_z(\cdot, t = 0) &= 0. \end{aligned} \tag{3.1}$$

Since the single mode indicates a frequency with a magnitude  $\lambda^* = \sqrt{(l)^2 + (\bar{m})^2 + (\bar{n})^2} = \sqrt{3}\pi$ , the exact solution of the Maxwell equation with the above initial data can be determined by a careful calculation:

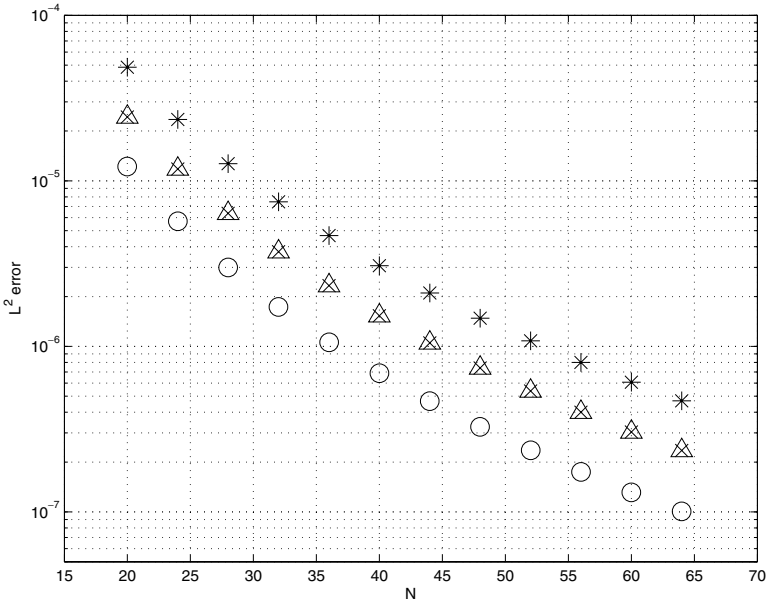
$$\begin{aligned} E_x &= \sqrt{u} \cos(\lambda^*t) \cos(\pi x) \sin(\pi y) \sin(\pi z), & E_y &= 0, \\ E_z &= -\sqrt{u} \cos(\lambda^*t) \sin(\pi x) \sin(\pi y) \cos(\pi z), \\ H_x &= \frac{\sqrt{3}}{3} \sqrt{\epsilon} \sin(\lambda^*t) \sin(\pi x) \cos(\pi y) \cos(\pi z), \\ H_y &= -\frac{2\sqrt{3}}{3} \sqrt{\epsilon} \sin(\lambda^*t) \cos(\pi x) \sin(\pi y) \cos(\pi z), \\ H_z &= \frac{\sqrt{3}}{3} \sqrt{\epsilon} \sin(\lambda^*t) \cos(\pi x) \cos(\pi y) \sin(\pi z). \end{aligned} \tag{3.2}$$

For simplicity, we take  $N_x = N_y = N_z = N$  so that the grid size is determined by  $h = \frac{1}{N}$ . We compute solutions with grid sizes 20 : 4 : 64 until a final time  $t = 4$ , using the proposed fourth order difference scheme over the Yee grid in conjunction with the Jameson time stepping. The ‘‘symmetric image’’ extrapolation for  $\mathbf{E}$  and  $\mathbf{H}$  is utilized. The time step  $\Delta t$  is set to be  $\Delta t = 0.5\Delta x$ , which satisfies the condition (3.38).

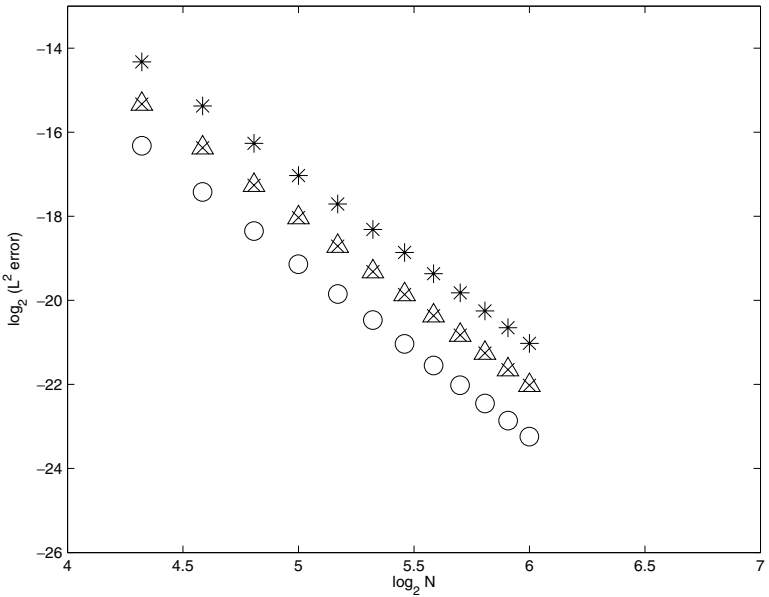
Figures 3 and 4 present the  $L^2$  and  $L^\infty$  norm of the errors between the numerical and exact solutions for all components of electric and magnetic field vectors. Part (a) shows the error for different values of  $N$ , while Part (b) gives the plot of these values on a base 2 log – log scale. The  $L^p$  norm is defined by

$$\|f\|_{L^p} = \left( \int_{\Omega} |f|^p dx \right)^{\frac{1}{p}}, \quad \text{for } 1 \leq p < \infty, \tag{3.3a}$$

$$\|f\|_{L^\infty} = \max_{\mathbf{x} \in \Omega} |f(\mathbf{x})|. \tag{3.3b}$$

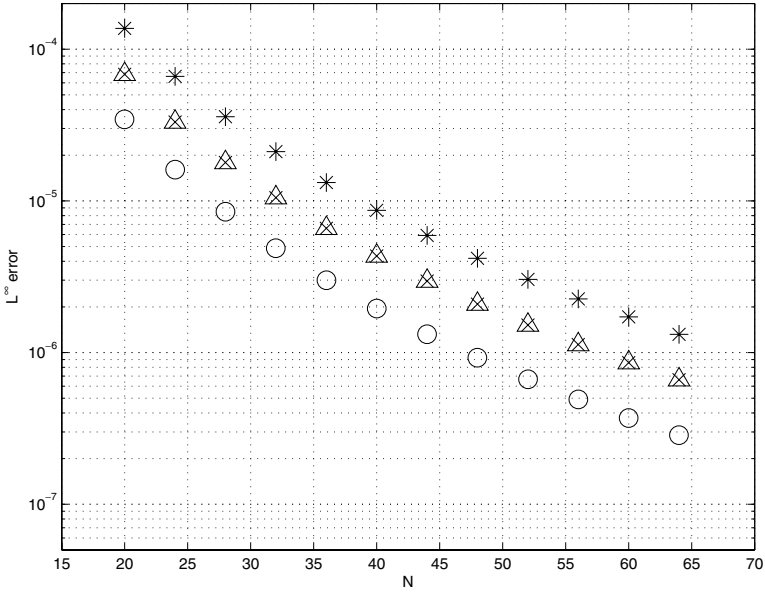


(a)

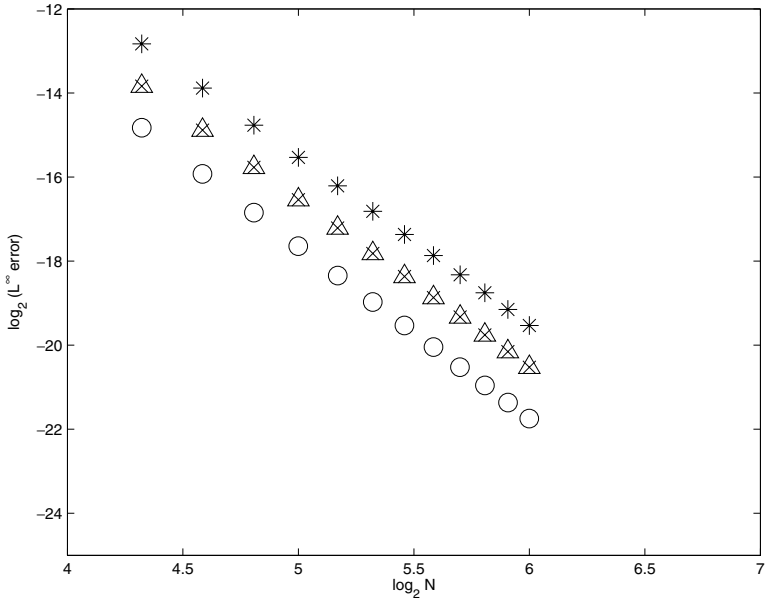


(b)

Fig. 3.  $L^2$  error of the fourth order *FDTD* method for the Maxwell equations: (a): the error versus the number of grid points  $N$ ; (b): plot of these values on a base 2 log – log scale. The final time is taken to be 4.0. The circle line represents the error of the  $E_x$  variable, the triangle line represents that of the  $H_x$  variable, the star line represents that of the  $H_y$  variable, and the cross line represents that of the  $H_z$  variable. Parameter:  $\mu = \epsilon = 1$ ,  $\Delta t = 0.5\Delta x$ .



(a)



(b)

Fig. 4.  $L^\infty$  error of the fourth order *FDTD* method for the Maxwell equations: (a): the error versus the number of grid points  $N$ ; (b): plot of these values on a base 2 log – log scale. The final time is taken to be 4.0. The circle line represents the error of the  $E_x$  variable, the triangle line represents that of the  $H_x$  variable, the star line represents that of the  $H_y$  variable, and the cross line represents that of the  $H_z$  variable. Parameter:  $\mu = \epsilon = 1$ ,  $\Delta t = 0.5\Delta x$ .

The numerical results provide clear evidence that the scheme is stable, and a fourth order accuracy in both space and time is apparently observed for all physical variables at a fixed final time. In particular, a full fourth order accuracy of the  $L^\infty$  errors shows that the “symmetric image” extrapolation formula does not cause any loss of accuracy.

### 5. A Benchmark Computation: Simulations of a Lossless Rectangular Cavity

To analyze and compare the performance of the  $2 \times 2$ ,  $2 \times 4$ , and  $4 \times 4$  numerical schemes, a rectangular metallic cavity was simulated. The dimensions of the cavity were chosen to be 1 m by 1 m by 1 m. Such a cavity can support an infinite number of eigen-modes, all of which are known from theory. This makes the rectangular cavity an ideal benchmark problem. Each mode has a corresponding resonant frequency, which is also known from theory to be  $\frac{1}{2}c\sqrt{l^2 + m^2 + n^2}$ , where  $l, m$ , and  $n$  are non-negative integers and at least two are nonzero. Here, the physical values of  $\mu = 1.257 \times 10^{-6}$  and  $\epsilon = 8.854 \times 10^{-12}$  were used.

The initial condition was chosen to force the initial magnetic field to be zero, and the initial electric field to be

$$\begin{aligned} \mathbf{E}(\cdot, t = 0) &= \sum_{l,m,n} A_{l,m,n} \mathbf{E}_{l,m,n}^0, \quad \text{with} \\ (E_x)_{l,m,n}^0 &= \cos(l\pi x) \sin(m\pi y) \sin(n\pi z), \\ (E_y)_{l,m,n}^0 &= -\frac{1}{2} \sin(l\pi x) \cos(m\pi y) \sin(n\pi z), \\ (E_z)_{l,m,n}^0 &= -\frac{1}{2} \sin(l\pi x) \sin(m\pi y) \cos(n\pi z). \end{aligned} \tag{3.1}$$

A simple calculation shows that  $\mathbf{E}$  and  $\mathbf{H}$  are divergence free and satisfy the boundary conditions at the cavity walls. For the trial simulation, the  $l = 3, m = 3, n = 3$  mode was used. This mode is a good test of the fourth order scheme because it has rapidly varying fields in the  $x$ -,  $y$ -, and  $z$ -directions. The theoretical resonant frequency is 778.88 MHz. In addition to this single mode initial condition, a multi-mode initial condition was also tested. It consists of a superposition of modes with different  $l, m$ , and  $n$  values. Again, the frequency of the mode  $l = 3, m = 3, n = 3$  was measured. The amplitude of each mode in the initial condition was given by

$$A_{l,m,n} = \frac{1}{l^2 + m^2 + n^2}, \quad \text{for } 1 \leq l, m, n \leq 20. \tag{3.2}$$

The accuracy of the simulations was measured by taking a dot product of the cavity fields with the known modal distribution of the  $3 \times 3 \times 3$  mode at each time step, in effect selecting only the mode of interest. An *FFT* is then performed with an appropriate window function, in this case a raised cosine function. Then, the

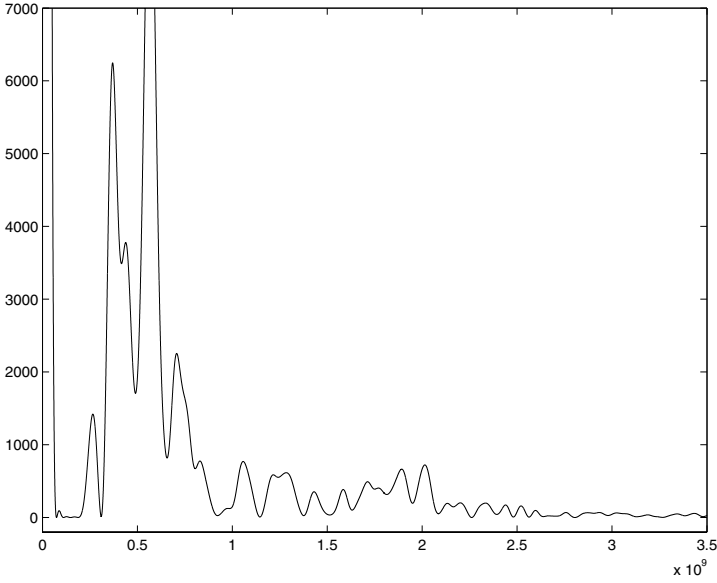


Fig. 5. Spectrum distribution at the sample point  $(\frac{1}{7}, \frac{1}{7}, \frac{1}{7})$ . The numerical results are based on the proposed fourth order scheme.

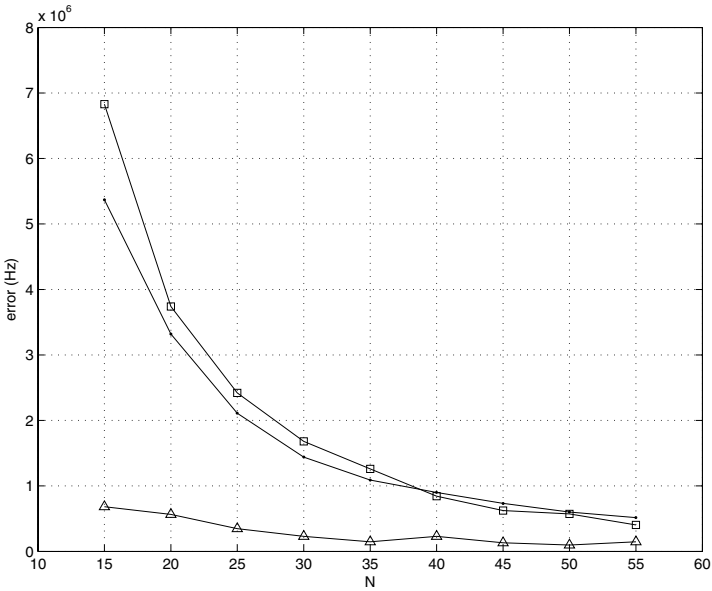


Fig. 6. Comparison between the proposed fourth order scheme with the classical  $2 \times 2$  and  $2 \times 4$  scheme. The phase errors for the  $l = 3, m = 3, n = 3$  mode, between the numerical simulations and the exact profile, are plotted. The dot line represents the error of the  $2 \times 2$  method, the square line represents that of the  $2 \times 4$  method, the triangle line represents that of the proposed fourth order method.

frequency of the peak in the Fourier power spectrum is compared to the known resonant frequency. A number of simulations were performed for each scheme, with different numbers of grid points, hence varying  $\Delta x$  (with the assumption  $\Delta x = \Delta y = \Delta z$ ).  $\frac{\Delta t}{\Delta x}$  was fixed by the most restrictive *CFL* condition (the  $2 \times 4$  case). The final time was also fixed.

We collect the data at a fixed sample point and compute the frequency of each mode. The spectrum distribution (computed by the  $4 \times 4$  method) is shown in Fig. 5.

Its comparison with the  $2 \times 2$  and  $2 \times 4$  schemes, regarding the frequency of the mode  $l = 3, m = 3, n = 3$ , is given in Fig. 6.

It is obvious that the the proposed fourth order method provides much more accurate simulation results than those of the  $2 \times 2$  and  $2 \times 4$  methods. Such an accuracy can even be observed for a relatively course mesh. For a  $20 \times 20 \times 20$  grid, for example, an error of 632 kHz is observed. By comparison, a  $50 \times 50 \times 50$  grid in *CST*, a commercial *FDTD* electromagnetic simulation software, gives an error of 1.15 MHz.

## References

- [1] G. Cohen and P. Joly, Construction and analysis of fourth-order finite difference schemes for acoustic wave equation in non-homogeneous media, *SIAM J. Numer. Anal.* **33** (1996) 1266–1302.
- [2] J. Fang, Time domain finite difference computation for Maxwell equations, Ph.D dissertation, University of California, Berkeley (1989).
- [3] S. Georgakopoulos, C. Birtcher, C. Balanis and R. Renaut, Higher order finite difference schemes for electromagnetic radiation, scattering, and penetration. Part 1: Theory, *IEEE Antenna's Propagation Mag.* **44** (2002) 134–142.
- [4] S. Georgakopoulos, C. Birtcher, C. Balanis and R. Renaut, Higher order finite difference schemes for electromagnetic radiation, scattering, and penetration. Part 2: Applications, *IEEE Antenna's Propagation Mag.* **44** (2002) 92–101.
- [5] F. H. Harlow and J. E. Welch, Numerical calculation of time-dependent viscous incompressible flow of fluid with free surface, *Phys. Fluids* **8** (1965) 2182–2189.
- [6] J. S. Hesthaven, *Advances in Imaging and Electron Physics* (Elsevier, USA, 2003).
- [7] A. Jameson, W. Schmidt and E. Turkel, Numerical solution of the Euler equations by finite volume methods using Runge–Kutta time stepping schemes, *AI AA Paper* (1981) 81-1259.
- [8] A. Jameson and P. D. Lax, Conditions for the construction of multi-point total variation diminishing difference schemes, *Appl. Numer. Math.* **2** (1986) 335–345.
- [9] S. K. Lele, Compact finite-difference schemes with spectral-like resolution, *J. Comput. Phys.* **103** (1992) 16–42.
- [10] J.-G. Liu, C. Wang and H. Johnston, A fourth order scheme for incompressible Boussinesq equations, *J. Sci. Comput.* **18** (2003) 253–285.
- [11] P. G. Petropoulos, Phase error control of *FDTD* methods of second and fourth order accuracy, *IEEE Trans. Antennas Propagation* **42** (1994) 859–862.
- [12] P. G. Petropoulos and A. Yefet, Subgridding a fourth order *FDTD* scheme for Maxwell's equations, in *Proceedings of Fourth International Workshop on Computational Electro-magnetics in the Time-Domain: TLM/FDTD and Related Techniques (CEM – TD)* (2001), pp. 39–45.

- [13] P. G. Petropoulos, L. Zhao and A. C. Cangellaris, A reflection-less sponge layer absorbing boundary condition for the solution of Maxwell's equations with high-order staggered finite difference schemes, *J. Comput. Phys.* **139** (1998) 184–208.
- [14] R. Samelson, R. Temam, C. Wang and S. Wang, A fourth order numerical method for the planetary geostrophic equations with inviscid geostrophic balance, to appear in *Numer. Math.*
- [15] J. S. Shang, High order compact difference schemes for time-dependent Maxwell equations, *J. Comput. Phys.* **153** (1999) 312–333.
- [16] A. Taflove, *Computational Electrodynamics: The Finite-Difference Time-Domain Method* (Aztech House, Boston, 1995).
- [17] A. Taflove, *Advances in Computational Electrodynamics: The Finite-Difference Time-Domain Method* (Aztech House, Boston, 1998).
- [18] E. Turkel and A. Yefet, On the construction of a high-order difference scheme for complex domains in a Cartesian grid, *Appl. Numer. Math.* **33** (2000) 113–124.
- [19] C. Wang, J.-G. Liu and H. Johnston, Analysis of a fourth order finite difference method for incompressible Boussinesq equations, *Numer. Math.* **97** (2004) 555–594.
- [20] Z. Xie, C.-H. Chan and B. Zhang, An explicit fourth order staggered finite-difference time-domain method for Maxwell's equations, *J. Comput. Appl. Math.* **147** (2002) 75–98.
- [21] Z. Xie, C.-H. Chan and B. Zhang, An explicit fourth order orthogonal curvilinear staggered-grid *FDTD* method for Maxwell's equations, *J. Comput. Phys.* **175** (2002) 739–763.
- [22] K. S. Yee, Numerical solution of initial boundary value problems involving Maxwell's equations in isotropic media, *IEEE Trans. Antennas Propagation* **14** (1966) 302–307.
- [23] A. Yefet and P. G. Petropoulos, Fourth order compact implicit method for the Maxwell equations with discontinuous coefficients, *Appl. Numer. Math.* **33** (2000) 125–134.
- [24] A. Yefet and P. G. Petropoulos, A staggered fourth-order accurate explicit finite differences scheme for the time-domain Maxwell's equations, *J. Comput. Phys.* **168** (2001) 286–315.
- [25] J. Young, The design of high-order, leap-frog integrators for Maxwell equations, *Antennas Propagation Soc. Int. Symp. IEEE* **1** (1999) 176–179.
- [26] J. Young, D. Gaitonde and J. Shang, Toward the construction of a fourth-order difference scheme for transient EM wave simulation: Staggered grid approach, *IEEE Trans. Antennas Propagation* **45** (1997) 1573–1580.
- [27] T. Zygidis and T. Tsiboukis, Optimized three-dimensional *FDTD* discretizations of Maxwell's equations on Cartesian grids, to appear in *J. Comput. Phys.* (2007).